

Development of a processing map for safe flash sintering of gadolinium-doped ceria

Tarini Prasad Mishra^{1,2}  | Christian Lenser¹  | Rishi Raj²  | Olivier Guillon^{1,4}  | Martin Bram^{1,3} 

¹Institute of Energy and Climate Research: Materials Synthesis and Processing (IEK-1), Forschungszentrum Jülich GmbH, Jülich, Germany

²Materials Science and Engineering Program, Department of Mechanical Engineering, University of Colorado Boulder, Boulder, Colorado, USA

³Institut für Werkstoffe, Ruhr-Universität Bochum, Bochum, Germany

⁴Jülich Aachen Research Alliance, JARA-Energy, Jülich, Germany

Correspondence

Tarini Prasad Mishra, Materials Science and Engineering Program, Department of Mechanical Engineering, University of Colorado Boulder, Boulder, CO, USA.
 Email: t.mishra@fz-juelich.de

Funding information

Deutsche Forschungsgemeinschaft, Grant/Award Number: BR 3418/1-1 and BR 3418/1-2

Abstract

Flash sintering was discovered in 2010, where a dog-bone-shaped zirconia sample was sintered at a furnace temperature of 850°C in <5 s by applying electric fields of ~100 V cm⁻¹ directly to the specimen. Since its discovery, it has been successfully applied to several if not all oxides and even ceramics of complex compositions. Among several processing parameters in flash sintering, the electrical parameters, i.e., electric field and electric current, were found to influence the onset temperature for flash and the degree of densification respectively. In this work, we have systematically investigated the influence of the electrical parameters on the onset temperature, densification behavior, and microstructure of the flash sintered samples. In particular, we focus on the development of a processing map that delineates the safe and fail regions for flash sintering over a wide range of applied current densities and electric fields. As a proof of concept, gadolinium-doped ceria (GDC) is shown as an example for developing of such a processing map for flash sintering, which can also be transferred to different materials systems. Localization of current coupled with hot spot formation and crack formation is identified as two distinct failure modes in flash sintering. The grain size distribution across the current localized and nominal regions of the specimen was analyzed. The specimens show exaggerated grain growth near the positive electrode (anode). The region adjacent to the negative electrodes (cathode) showed retarded densification with large concentration of isolated pores. The electrical conductivity of the flash sintered and conventional sintered samples shows identical electrical conductivity. This quantitative analysis indicates that similar sintering quality of the GDC can be achieved by flash sintering at temperature as low as 680°C.

KEY WORDS

conductivity, flash sintering, gadolinium-doped ceria, hot-spot generation, microstructure, processing map

This is an open access article under the terms of the Creative Commons Attribution-NonCommercial License, which permits use, distribution and reproduction in any medium, provided the original work is properly cited and is not used for commercial purposes.

© 2021 The Authors. *Journal of the American Ceramic Society* published by Wiley Periodicals LLC on behalf of American Ceramic Society (ACERS)

1 | INTRODUCTION

Gadolinium-doped ceria (GDC) has a wide range of applications, especially in environmental and energy technologies.¹ It has remarkable redox and oxygen storage capability (OSC).² Thus, it is used as a catalyst, or as a catalyst support for chemical processing.^{3–5} It also possesses high ionic conductivity between 500 and 600°C,^{6,7} which makes it a strong candidate for electrochemical devices like oxygen sensors,^{8,9} oxygen transport membranes,^{10,11} cermet electrodes,^{12–14} and electrolytes for solid oxide fuel and electrolysis cells (SOFC/SOECs).^{6,7,15,16}

However, conventional sintering of GDC entails high temperatures (1300–1600°C) and dwell times of several hours in air to achieve density >96%.^{17,18} Lowering the sintering temperature would be advantageous for fabricating dense GDC from the energy consumption perspective. To a limited degree, the reduction of sintering temperature can be achieved by reducing the particle size,^{16,19} adding sintering aids,^{20,21} or processing under reducing atmosphere.^{22–24} But nano-sized powder is difficult handle with respect to agglomeration and may not be cost effective for large-scale production. The sintering aids may deteriorate the electrochemical properties,²⁵ and using reducing atmosphere requires re-oxidation at a high temperature to reliably avoid the microcracking.^{24,26}

Recent advancements in electric current activated/assisted sintering techniques (ECAS) are shown to be promising for the processing of advanced materials due to significant enhancement of densification kinetics at lower furnace temperatures, when compared with conventional sintering technologies.^{27–30} Technologies like, Spark Plasma Sintering (SPS) also referred in the literature as Field Assisted Sintering/Spark Plasma Sintering (FAST/SPS)²⁹ or flash sintering^{31,32} are attractive due to the lower furnace temperature and shorter dwell time required for fabricating dense materials. The use of high heating rates and shorter dwelling time in these processing routes offers the possibilities of tuning microstructures down to the nanoscale. FAST/SPS is a low-voltage, direct current (DC) pulsed-activated pressure-assisted technique. It can be used for sintering as well as for material synthesis.

Although many ceramics were successfully consolidated by FAST/SPS, sintering of some oxides remains a challenging task. An example is sintering of ceria (CeO_2) and doped ceria, which is an excellent mixed ionic-electronic conductor with a great potential for application in electrochemical devices. The main problem is fracture of fully dense or nearly dense sintered ceria and doped ceria samples.^{33,34} The state of the art for processing GDC by FAST/SPS and specific challenges are discussed in depth elsewhere.^{26,34} The use of graphite dies causes localized heterogeneous reduction of GDC, which is spatially dispersed. It has been observed that the loss of oxygen is most severe at the interface in direct

contact with the electrodes. On a macroscopic scale, samples fracture into several pieces during ejection from the die. Inhomogeneous chemical expansion, induced by non-uniform reduction of the sample leads to internal stresses causing this phenomenon.^{26,35} The chemical expansion of GDC is related to the volume expansion and contraction with oxygen depletion and accumulation in the lattice, respectively.²⁶ The degree of chemical expansion is associated with the electrochemical potential of oxygen in the lattice, which is a function of the partial pressure of oxygen, temperature and the electrical potential. More recently flash sintering, discovered in 2010, has been shown to sinter zirconia at a furnace temperature of 850°C in <5 s by applying electric fields of ~100 V cm⁻¹ directly to the specimen.³⁶ Since its discovery, flash sintering has been shown to apply to several if not all oxides and even ceramics of complex compositions.^{32,37–40} Voltage and current control are prerequisite for reliably conducting this process. The flash experiments can be carried out in two modes, the voltage-to-current control modus,^{32,41–44} and the current-rate control modus.^{45–48} Most experiments were carried out in the first mode so far, where an electric field is applied to a powder-pressed “green specimen” held at a certain furnace temperature or by ramping up the furnace temperature at a constant rate. These variants are known as isothermal flash sintering and constant heating rate flash sintering, respectively.

Depending on the material, flash is initiated by a specific combination of electric field and furnace temperature, also known as onset of flash.⁴⁹ It is signaled by a non-linear rise in material conductivity, and a surge in power dissipation. After initiating the flash event, the specimen sinters to nearly full density, typically within seconds. The surge is contained by switching the power supply from voltage control to current control. The current limit determines the extent of sintering.⁵⁰ Thus, the flash sintering process has the following characteristics: (a) nonlinear rise in the conductivity,^{36,39} (b) bright light emission,^{51–53} and (c) rapid densification.^{54,55} Furthermore, the Debye temperature is currently seen as a lower bound temperature for the onset of flash.^{49,53,56} However, the underlying mechanisms for the flash sintering process remain under consideration.^{44,57–64}

Previous studies demonstrated that flash sintering of GDC can produce densities of ~95% at a furnace temperature of 500–900°C, in just a few seconds.^{48,65–68} However, some experiments suggested that flash sintered GDC samples still retained porosity hinting on not-optimum flash conditions.⁶⁶ Also, a systematic investigation of microstructure evolution remained incomplete. Therefore, the objective of this work is to systematically study the influence of the electrical parameters on densification behavior and microstructure evolution. A processing map, that specifies the “SAFE” and “FAIL” regimes as a function of current densities and electric fields, is developed. Two failure mechanisms, current localization

coupled with hot spot formation and fracture due to pronounced cracking were identified. The microstructure at different regions of the flash sintered sample was characterized. In addition, the electrical conductivity of the flash sintered sample from the safe regime was measured. The electrical conductivity of the flash sintered sample was compared with a conventionally sintered sample with similar relative density.

2 | EXPERIMENTAL PROCEDURE

2.1 | Material system

Commercially available 10 mol% GDC (GDC10, $\text{Gd}_{0.10}\text{Ce}_{0.90}\text{O}_{1.95}$) powder (grade GDC10-HP, Fuel Cell Materials, USA) was used as the starting material. Particle size distribution was measured with the laser diffraction method (LA-950-V2, Horiba Ltd.) resulting in a $d_{10} = 0.07 \mu\text{m}$, $d_{50} = 0.13 \mu\text{m}$, and $d_{90} = 1.97 \mu\text{m}$. This means that the maximum particle diameters being less than 10%, 50%, and 90% of the cumulative volume. The starting powder had a bimodal distribution, suggesting the presence of some agglomerates. The specific surface of the starting powder was $10.5 \text{ m}^2 \text{ g}^{-1}$ (Area Meter II, Ströhlein Instruments). The measured particle size distribution, X-ray diffraction analysis, SEM, and TEM images are presented in Figure 1.

The as received powder was mixed with a 2-wt% organic binder Duramax B-1000 (Rohm and Haas France SAS, BP). This aqueous emulsion was used as binding agent. The binder mixed powder was then uniaxially pressed in a dog-bone

shaped die with a pressure of 100 MPa. The dog-bone had a gauge length of 15 mm, a width of 3.3 mm, and a thickness between $1.95 \pm 0.15 \text{ mm}$. The amount of powder used for these specimens was $1.0 \pm 0.1 \text{ g}$. The green body samples were too fragile to connect to the electrodes. Therefore, they were heated to 600°C for 1 h to remove the binder, and then pre-sintered at 1000°C for 30 min with a heating and cooling ramp of 3 K min^{-1} . The relative densities of the pre-sintered samples, measured geometrically, was approximately $62 \pm 1.5\%$.

2.2 | Flash sintering set-up and procedure

The dog-bone-shaped samples were connected to the power source with a pair of platinum wires. Platinum paste was applied to ensure good electrical contact. The flash sintering experiments were carried out in a vertical tubular furnace; the experimental set-up is shown elsewhere.⁶⁹ Electric field was applied using a Glassman 3-kW DC power source (Glassman High Voltage Inc.) with a maximum voltage of 2000 V. For electric fields above 2000 V cm^{-1} , the gauge length was shortened. The current flowing through the sample was measured with a digital multi-meter (Keithley 2000, Keithley Instruments). The communication and control of the power supplies were achieved by data acquisition (DAQ) devices USB-6008 (National Instruments). General Purpose Interface Bus (GPIB) was used to communicate with the multimeter; the device that monitors the current was the multimeter itself. Data were acquired through a graphical user

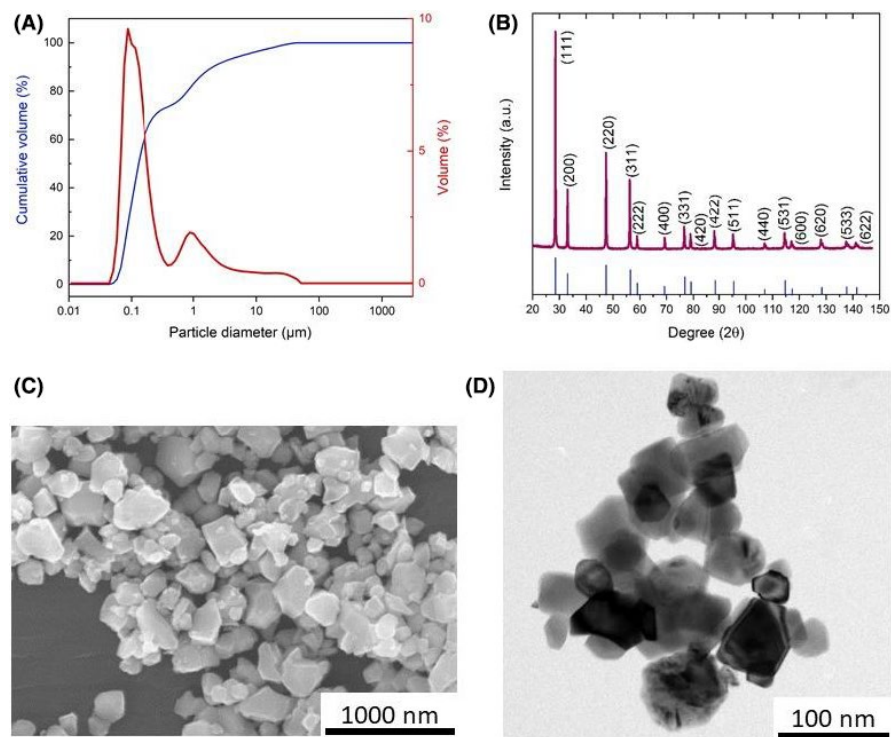


FIGURE 1 Starting powder characterization: (A) particle size distribution, (B) X-ray diffraction spectra, (C) SEM micrograph, and (D) TEM micrograph [Color figure can be viewed at wileyonlinelibrary.com]

interface (GUI) developed in-house (University of Colorado Boulder), running on MATLAB program.

The pre-sintered dog-bone-shaped sample was placed in the tubular furnace with the two platinum electrodes wires. Voltage-to-current experiments were performed with a constant heating rate of $10^{\circ}\text{C min}^{-1}$. A constant electric field was applied at room temperature, and the furnace was then heated at this rate. Just after the onset of flash, the power supply was switched from voltage-to-current control. The sample was held under current control for 30 s before the power was switched off. In isothermal flash sintering experiments, the furnace temperature was held constant; the sample remained in the furnace for 10 min to achieve a uniform temperature, and then the electric field was applied. Again the power supply was switched to current control just after the onset of the flash. The power was switched off after being held for 30 s at the maximum current density.

The shrinkage of the sample was monitored by a digital charge-coupled device (CCD) camera. The true uniaxial shrinkage, ϵ , was measured continuously from photographs taken at 1-s intervals. The linear shrinkage strain, ϵ , is given by

$$\epsilon = \ln(L/L_0), \quad (1)$$

where L_0 and L are the initial and the time dependent gauge lengths. Note that the strain is a negative quantity.

The gauge section of the flash sintered samples were used for all characterizations. The final relative density of the sintered samples was measured by the Archimedes' principle with distilled water as a liquid medium. The values for the relative densities were calculated assuming a theoretical density for GDC10 of 7.22 g cm^{-3} . Investigation of microstructure was performed on the cross-sections (in length direction) of samples after polishing according to a standard sample preparation process. The surfaces were thermally etched by annealing at 1250°C for 20 min, to delineate the grain boundaries. SEM images of the sputter-coated (platinum) microstructures were taken with a table top SEM (Phenom, Fei Company).

2.3 | Impedance spectroscopy

Impedance spectra in the frequency range of 10^6 to 10^{-1} Hz were recorded using an Alpha-A High performance Frequency Analyzer (Novocontrol Technologies GmbH) in a tube furnace in air in the temperature range between 200 and 600°C . The spectral quality was evaluated using the Kramers–Kronig transformation, performed with the Lin-KK software tool.⁷⁰ Silver electrodes painted onto the sample were used to ensure good contact to the Pt wires of the setup. The measurement temperature was limited to 600°C to avoid excessive sublimation of the Ag

electrodes. Complex nonlinear least squares (CNLS) fitting to an equivalent circuit model was performed with ZView (Scribner Associates Inc). Each contribution in the spectrum was modeled by a parallel circuit of a resistance and a constant phase element (CPE) with $Z = 1/(j\omega Q)^{\alpha}$.

Impedance spectra were recorded on a representative flash sintered (isothermal) sample from the “safe” regimes in the processing map. The sample was flash sintered at a constant furnace temperature of 680°C and a DC electric field of 90 V cm^{-1} . The maximum current density of 200 mA mm^{-2} was applied for 30 s after the onset of flash. For comparison, a reference sample was produced from the same powder batch by uniaxial pressing in a cylindrical die of 20 mm diameter at a pressure of 150 MPa, and subsequent sintering at 1400°C for 2 h in air. For the reference sample, Ag electrodes were fabricated using the same Ag paste as for the Flash sample. The conductivity of the grains (σ_g) and grain boundaries (σ_{gb}) was calculated via:

$$\sigma_g = \frac{L}{R_g \cdot A},$$

$$\sigma_{gb} = \frac{L}{R_{gb} \cdot A} \cdot \frac{C_g}{C_{gb}}.$$

The ratio of the respective pseudocapacitances of the grain and grain boundary impedances, C_g and C_{gb} , respectively, was used as a geometrical correction factor to account for the much smaller grain boundary volume. The pseudocapacitance for each CPE was calculated via:

$$C = R^{\frac{1-\alpha}{\alpha}} \cdot Q^{\alpha}.$$

3 | RESULTS AND DISCUSSION

The onset temperature of flash depending on the electric field is shown in Figure 2A. In agreement with other flash experiments, the flash temperature decreases with increasing electric field. However, once the field reaches 1000 V cm^{-1} , the onset temperature appears to approach an asymptotic value. Indeed at a much higher field of $>3000 \text{ V cm}^{-1}$, the onset temperature saturates at approximately 150°C .

Visual inspection of the samples, which were flash sintered above an electric field of 300 V cm^{-1} revealed the formation of cracks. At very high electric fields ($>1000 \text{ V cm}^{-1}$), the samples splintered into many small pieces, even at very low currents (a few mA). The power density profile of the splintered samples showed a maximum value of 10 mW mm^{-3} ; therefore, it is safe to assume that the sample temperature was similar to the furnace temperature before the samples splintered. Similar cracking/splintering of the samples at higher electric field was also observed in dense GDC10 samples.⁴⁹

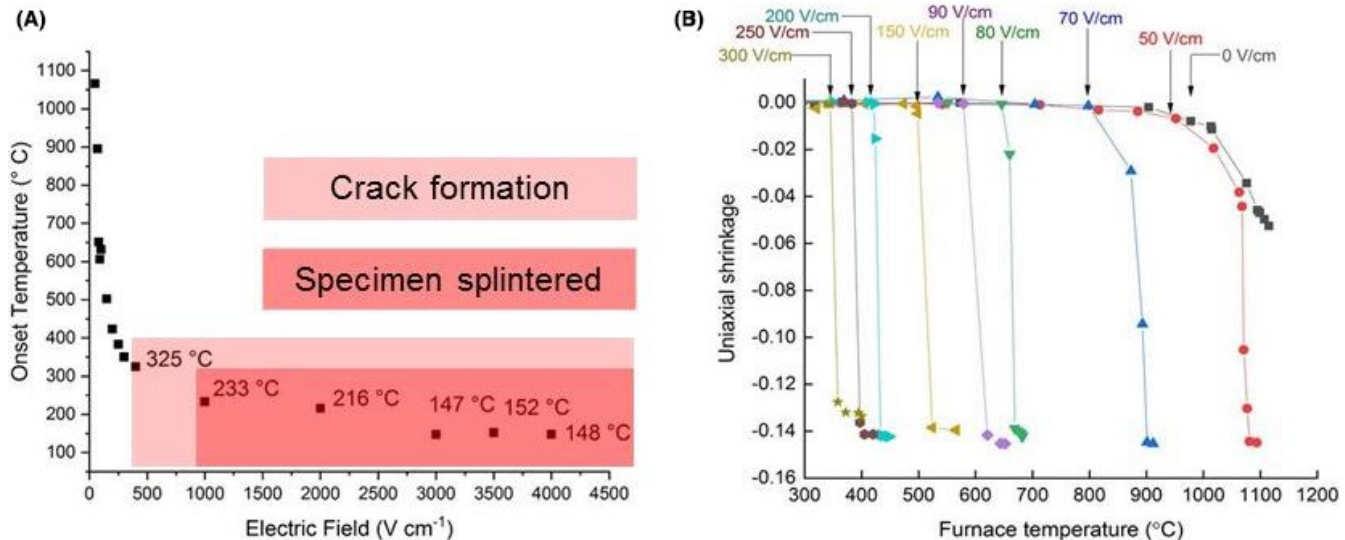


FIGURE 2 (A) The furnace temperature for the onset of the flash event as a function of electric field and (B) Uniaxial shrinkage during the constant heating rate experiments at different electric fields [Color figure can be viewed at wileyonlinelibrary.com]

The cracking of the samples at higher electric field may be related to the non-uniform lattice expansion associated with spatially non-uniform generation of oxygen vacancies. It is known that GDC expands upon reduction because the ionic radius of the cations increases from Ce⁴⁺ (0.907 Å) to Ce³⁺ (1.143 Å). Also, the positively charged oxygen vacancies are electrostatically repelled by the surrounding cations.^{26,71} First, the sample reduces adjacent to the cathode. Afterwards, the reduction front moved towards the anode. The movement of the reduction front may appear to be optically homogeneous at the macroscopic scale,⁷² but on microscopic scale, it maybe localized and heterogeneous.

Another possible reason for cracking/splintering of the samples might be a localized thermal shock. In the case of voltage-to-current flash sintering, the power surge happens quickly. At high fields and low furnace temperatures, the power surge can produce thermal gradients and thereby, heterogeneous stress distribution leading to mechanical failure of the samples.

In Figure 2B, the linear uniaxial shrinkage is plotted for electric fields ranging from 0 to 300 V cm⁻¹. Shrinkage at higher electric fields (above 300 V cm⁻¹) could not be measured because the samples were cracked. At 50 V cm⁻¹, the shrinkage behavior of GDC10 until onset of flash at around 1100°C coincides with the conventional densification rate without electric field. At electric fields above 70 V cm⁻¹, a rapid shrinkage can be observed in mere seconds. The relative density of all the samples was around 88%, as measured by the Archimedes' method. These results suggest that the current density of 100 mA mm⁻² is not enough to fully densify the GDC10 material. In comparison, full density in YSZ was already achieved at a current density of 100 mA mm⁻².⁵⁰

The optimum combination of furnace temperature and electric field for initiating flash was identified from constant heating rate experiments, based on the relative density of the flash sintered samples. These data were then used for isothermal voltage to current flash sintering experiments. These experiments were carried out at constant furnace temperature of 680°C and constant electric field of 90 V cm⁻¹. The influence of the current density on the degree of densification was studied (Figure 3).

The influence of the maximum current density on the relative density of flash sintered specimen is reported in Figure 3A. Higher current limit led to higher density as has been reported for other oxides.^{50,55,73} At 250 mA mm⁻², a density of around 97% was achieved. At higher current densities, the current began to “channel,” resulting in partial densification such that densification only occurred in a small area while the remaining area remained non-sintered. Further densification of the samples may be achieved by increment of the holding time at stage III at a current density between 200 and 250 mA mm⁻². Nevertheless, the microstructure of the samples shows that near the positive side the pores are entrapped inside the grains. These pores are impossible to eliminate further; however, the volume percentage of these pores in the sample is negligible for most of the technological applications. The microstructural effects of the failed specimens will be discussed later in this section.

The localization of the current represents a preferential path for current flow through the specimen. It is well established that the applied electric field results in the migration of oxygen vacancies to the negative and oxygen ions to the positive electrode. With respect to the applied electric field and time, the reduction front moves from the negative electrode towards the positive electrode.^{72,74} The move forward of the reduction front is not always homogeneous. It is assumed that

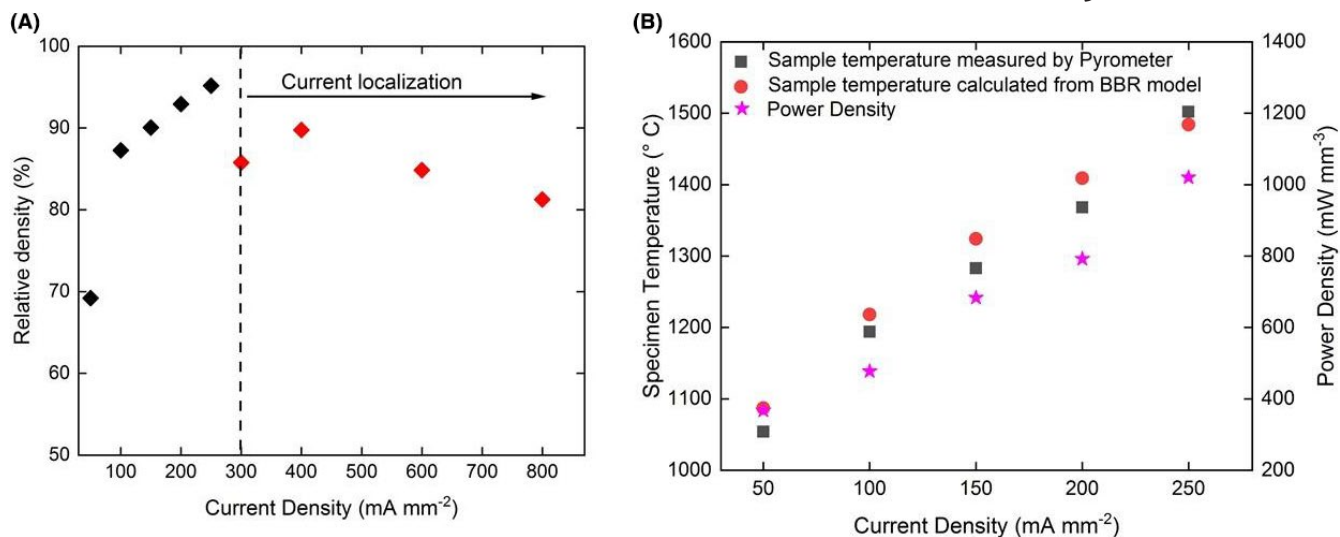


FIGURE 3 (A) The influence of current density on the degree of densification and (B) Specimen temperature measured by the pyrometer, calculated from the BBR model and the power density at stage III for different current densities, at constant electric field (90 V cm^{-1}) and furnace temperature (680°C) [Color figure can be viewed at wileyonlinelibrary.com]

on microscopic scale the reduction front may have a filament shaped appearance similar to the reaction front reported for memristor devices.^{75,76} The reduction of ceria generates oxygen vacancies and electrons to maintain the charge neutrality. According to density-functional theory (DFT) calculations of ceria surfaces, oxygen vacancies form preferentially on subsurface sites, and the two excess electrons tend to localize on next nearest neighbor Ce^{3+} ions.⁷⁷ This may enhance the electronic conductivity of the filament substantially as compared to the rest of the sample. The defect chemistry and related conductivity of GDC is extensively reported in the literature.^{6,78}

The specimen temperature during the quasi-steady state (stage III) of the isothermal flash sintering experiments was measured with an optical pyrometer and estimated by black body radiation (BBR) model from the power density. In a quasi-steady state of flash (Stage III in voltage-to-current experiments), the estimated sample temperature by BBR model match quite well with the pyrometer temperature. Direct measurement of the sample temperature with a platinum standard during in situ experiments at synchrotron facilities for TiO_2 and YSZ has been in good agreement with the BBR model and the pyrometer values.⁷⁹ During the quasi-steady state, BBR model assumes that the power consumption is equal to the radiation loss. The BBR model used in this study to estimate the sample temperature is reported elsewhere,⁸⁰ which is derived from the Stefan-Boltzmann law and modified for the flash experiment condition (Equation 2).

$$\frac{T}{T_0} = \left[1 + \frac{1000 * W_v}{\sigma T_0^4} \left(\frac{V}{A} \right) \right]^{1/4}. \quad (2)$$

In Equation 2, T is the sample temperature (K), T_0 the furnace temperature (K), A is the surface area (mm^2), V is the volume of the sample (mm^3), W_v is the normalized power dissipated in the sample with respect to the volume of the sample (W mm^{-3}), $\sigma = 5.670374419... \times 10^{-8} \text{ W} * \text{m}^{-2} * \text{K}^{-4}$ is the Stefan-Boltzmann constant and α is a correction factor to account the emissivity of the sample. In the current experiments, the emissivity of GDC10 was assumed to be 0.9.

The specimen temperature was measured with the pyrometer, and estimated from the BBR modal at the quasi-steady state (stage III). Results are given in Figure 3B. The figure also includes the corresponding power density at stage III. Both estimated and measured temperatures are in good agreement. Another remarkable result from this analysis is how accurately the sample temperature and the degree of densification of GDC10 matches with the conventional sintering result, which shown in Figure S1. In conventional free sintering, a temperature of 1400°C is required to achieve a relative density of approximately 95%. In the case of flash sintering, almost the same sample temperature was achieved mainly by Joule heating when applying a current density of 200 mA mm^{-2} , resulting again in a density of around 95%. Nevertheless, the sintering rate in conventional sintering is much lower and the dwell time much longer than in flash sintering.

Additionally, isothermal flash sintering experiments with a maximum current density of 200 mA mm^{-2} and variation of electric field were carried out. In these series of experiments, the sample cracked at lower electric field (250 V cm^{-1}) as compared to the constant heating rate experiments with a maximum current density of 100 mA mm^{-2} . Depending on their appearance, the samples were assigned to “SAFE” and “FAIL” conditions, and all results are compiled in a

processing map given in Figure 4. The axes of this map are the current density and the electric field.

The failure of flash sintered samples was categorized in two ways:

- Fracture: higher electric fields lower the onset temperature for the flash but do not affect the degree of densification. However, electric fields in the range 300–1000 V cm⁻¹

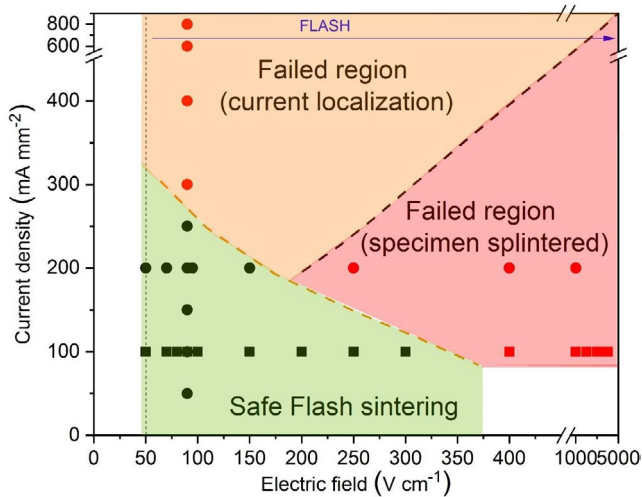
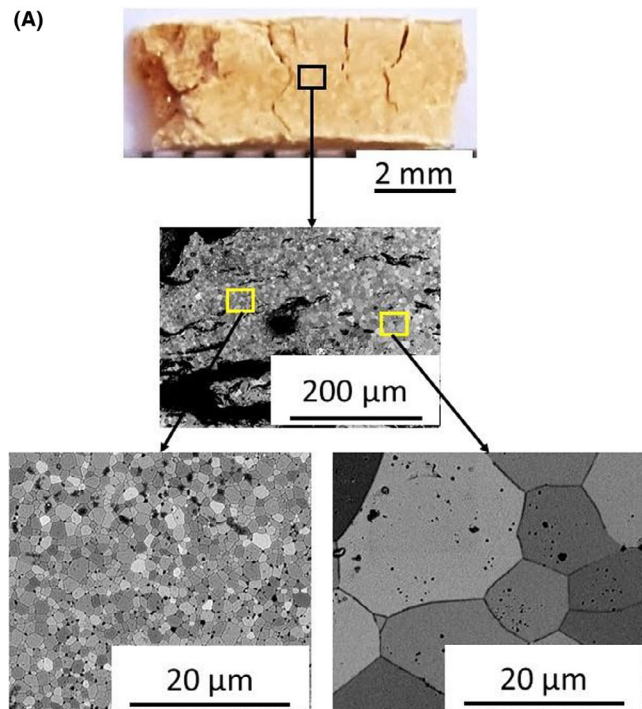


FIGURE 4 Processing map for voltage-to-current controlled flash sintering of GDC10. The rectangular and circular symbols denote the constant heating rate and isothermal flash sintering experiments, respectively [Color figure can be viewed at wileyonlinelibrary.com]



resulted in generation of cracked but still coherent samples, as shown in Figure 5A. Further increase of the electric field above 1000 V cm⁻¹ caused that specimen splintered into many small pieces.

- Current localization: the degree of densification depends on the current density. However, at very high current density, the current seems to localize along a preferential path in the specimen. An example of such localization in the flash sintered sample is shown in Figure 5B.

SEM micrographs of the failed flash sintered samples obtained from the polished and thermally etched surfaces are also shown in Figure 5. The microstructure of the sample with current localization confirming that the sample was only partially dense. In the non-sintered area, many pores remained, while in the area with current localization full densification and significant grain growth was observed. On the contrary, the failure mechanism was significantly different when caused by high electric fields. In this case, specimen showed localized damage.

The microstructure of the flash sintered samples processed under “SAFE” flash conditions was characterized at different positions along the gauge section is shown in Figure 6. The microstructures that are perpendicular to the direction of current flow revealed non-uniform grain size distribution in the gauge section of the sample. The grain size close to the surface were finer as compared to the grains in the middle part of the sample. The coarser grains

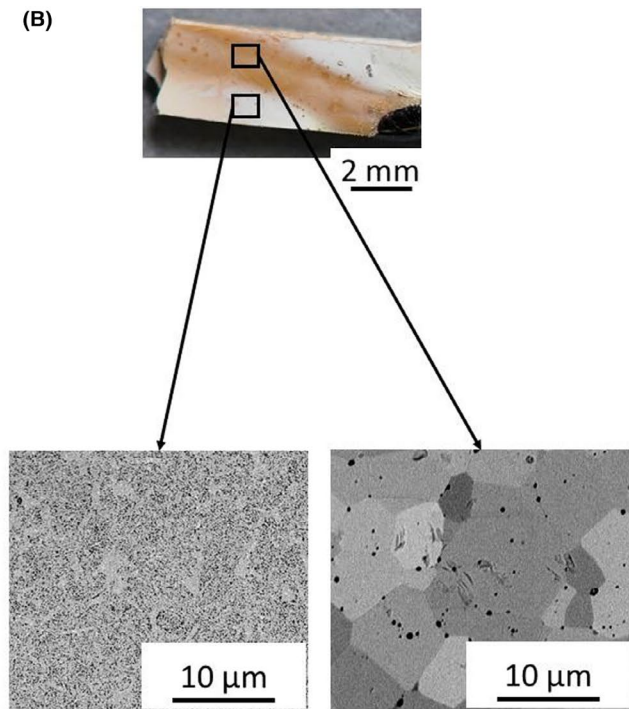


FIGURE 5 SEM microstructure analysis of samples failed due to (A) high electric field and (B) high current density [Color figure can be viewed at wileyonlinelibrary.com]

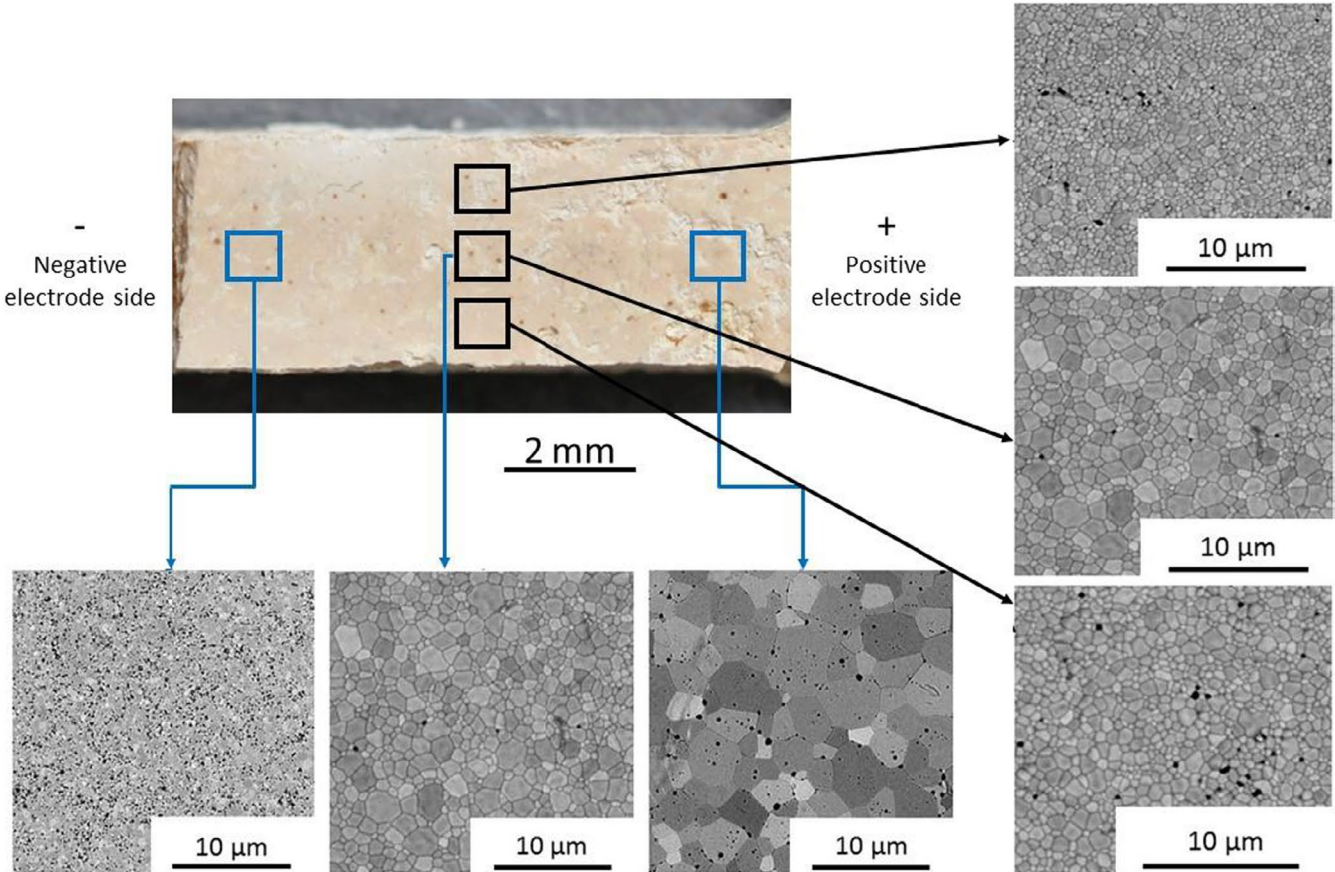


FIGURE 6 SEM micrographs at different positions of a sample belonging to the safe region. Flash sintering parameters: Isothermal flash sintering, furnace temperature 680°C, DC electric field 150 V cm⁻¹, maximum current density 200 mA mm⁻² and Holding time after the onset of flash 30 s [Color figure can be viewed at wileyonlinelibrary.com]

at the center suggest a higher local temperature. Previous empirical and modeling studies on the temperature distribution of the Zirconia samples during flash state reported non-uniform temperature distribution in the sample.^{81,82} They found significantly higher temperature in the middle section of the sample as compared to the top and bottom surfaces, presumably because of radiative thermal losses from the surface. The larger grain size in the core region is in agreement with our previous report on the current rate flash sintering of GDC10.⁴⁸

The grain size along the current flow direction, however, showed a large deviation. SEM micrographs of a flash sintered specimen (constant heating rate, 10°C min⁻¹, 150 V cm⁻¹, and 200 mA mm⁻²) at different positions along the gauge section and across the gauge section is shown in Figure 6. The average grain size near the anode was approximately 3 ± 1.1 μm, in the center 0.70 ± 0.35 μm and at the cathode 0.40 ± 0.23 μm. Furthermore, the microstructure near the cathode region revealed to retained close pores. The average grain size changed over a factor of ten from the anode to the cathode. Such non-uniformities in voltage-to-current flash experiments have been reported for other materials as well.^{46,47,83-85} However, in some cases coarser grains

are observed near the cathode, while in other materials, the coarser grains are near the anode.⁵⁸

The abnormal grain growth is often related to electrochemical effects induced by the application of DC electric field.^{44,72,74,86-89} Under DC electric field, oxygen vacancies ions will migrate and accumulated near the negative electrode (cathode), while the oxygen ions will migrate towards the positive electrode (anode). This results in enhanced oxygen ion concentration at the grain boundaries near the positive electrode region. This can alter the space charge region,⁹⁰ which may increase the grain boundary mobility thereby resulting in coarser grain size, as shown in Figure 6. Recent study on the densification and grain growth behavior of GDC10 sintered by FAST/SPS, where the net electric field was negligible as compared to the flash sintering conditions also showed enhanced grain growth regions close to the positive electrodes.³⁴

Nevertheless, the limited densification near the cathode region is likely related to the temperature gradient. The change in oxygen vacancies concentration results in charge compensation from electrons to conserve the electro-neutrality. This can influence the electrical conduction mechanism in the sample, where anodic and cathodic bulk

regions become primarily p-type and n-type. Charalambous and coworkers⁸⁴ proposed the abnormal grain growth in Titania near anode due to the Peltier effect, which causes heating at the anode-electrode junction and cooling at the cathode. In GDC10, significant electrochemical reduction at the cathode propagates to the anode.⁷² As the cathode side is reduced to a greater degree than the anode side, the interface resistance at the anode will be greater, causing local heating. The higher local temperature may then contribute to enhanced densification and higher rate of grain growth as compared to the cathode side.

The inhomogeneity in the microstructure during voltage-to-current flash sintering can be avoided by optimizing the processing parameters. For example, recent work from our group⁴⁸ showed that current rate flash sintering, where the power supply is always held under current control, the grain size was highly uniform across the full gauge section of the dog-bone specimens.

The fundamental explanation for this dichotomy between current-rate and voltage-to-current experiments is the difference in the current density at the onset of flash. In voltage-to-current flash sintering, the current density rises abruptly to the current limit which is often in the range of 50–200 mA mm⁻². These high currents can produce large voltage drops at the electrodes—given by the product of the current density and the charge transfer interface resistance—which produces local heating. Furthermore, the voltage drops can be large enough to produce redox reactions which can exacerbate the local heating particularly for the reduction reaction at the cathode. In contrast, in the current-rate experiments, the current density at the onset of flash for GDC10, as reported earlier,⁴⁸ was in the range of 7–9 mA mm⁻², which may reduce the voltage drop across the interface thereby sidestepping the reduction reaction.

Furthermore, Biesuz et al.⁸⁶ reported that the use of AC current for the flash sintering experiments can minimize such electrochemical effects. Additionally, different electrode materials act differently at the electrode and sample interface. Therefore, it is expected that the homogeneity of the sample can also be improved by using alternate electrode materials.

Figure 7 shows the total, grain and grain boundary conductivity vs. reciprocal temperature of the flash-sintered sample, and the conventionally sintered sample. The established equivalent circuit model for the impedance analysis of ionic conductors is the brick-layer model, which approximates both grain and grain boundary contributions as a parallel circuit consisting of one resistor and one CPE each. This model yields satisfactory results for the conventionally sintered ceramic and the flash sintered ceramic, when extended by R-CPE elements to describe the electrode response. A grain size analysis for a sample processed under identical conditions as the reference sample yielded an average grain size of 0.73 ± 0.3 μm, and the relative density was

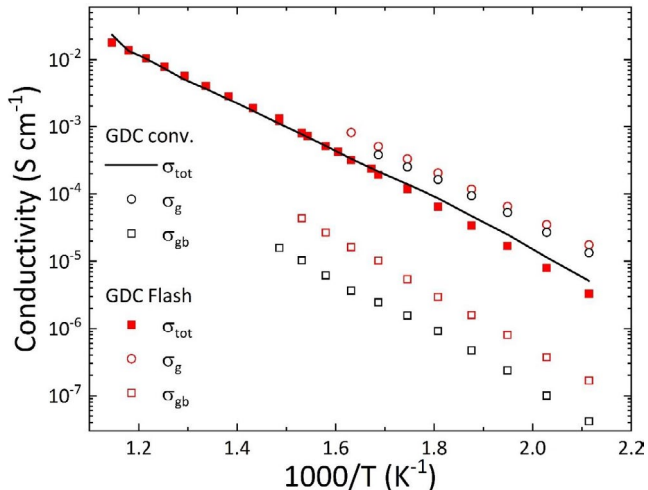


FIGURE 7 The total, grain and grain boundary conductivity vs. reciprocal temperature for the conventionally sintered gadolinium-doped ceria (GDC) sample (black line, open circles and squares, respectively) and for the Flash-sintered GDC sample (red solid squares, open circles and open squares, respectively). [Color figure can be viewed at wileyonlinelibrary.com]

determined as 97.9 + 0.2%.⁹¹ The values for total and grain conductivity of both samples are identical within the margin of error of the analysis, while the grain boundary conductivity of the flash sintered sample is somewhat higher than that of the conventionally sintered sample. The fitted values for the activation energy of each partial conductivity are shown in Table 1, along with the grain and grain boundary capacitances at 200°C. All values are within the expected range for GDC ceramics.^{78,91}

Further investigations are necessary to confirm whether the higher grain boundary conductivity is a result of the flash sintering. For the purpose of this investigation; however, the data clearly shows that the conductivity of the flash sintered sample is comparable to that of the sample prepared by conventional sintering.

4 | SUMMARY

In this work, flash sintering of GDC10 applying DC conditions was extensively studied. Based on the study, a processing map delineating the “SAFE” and “FAIL” regimes in terms of the current density and the electric field has been developed. Two distinct failure mechanisms were identified. In the case of very high current densities current localization occurred. Contrary, in the case of high electric fields, samples tend to crack and in worst case splinter into many pieces. Processing map of GDC10 for flash sintering will be beneficial for designing future flash sintering experiments, and failure of the sample can be avoided by avoiding the failed processing parameters. Such processing maps can also be developed for different material systems.

TABLE 1 Activation energy (EA) values, as well as pseudocapacitances for each component (at 200°C)

Sample	E_A , grains	C , grains	E_A , gb	C , gb	E_A , total
GDC conv.	0.68 ± 0.01	$8.8 \cdot 10^{-11}$ F	0.80 ± 0.003	$1.8 \cdot 10^{-8}$ F	0.72 ± 0.01
GDC Flash	0.66 ± 0.01	$4.3 \cdot 10^{-11}$ F	0.87 ± 0.03	$1.9 \cdot 10^{-9}$ F	0.81 ± 0.02

While higher electric fields lowered the flash-onset temperature, the degree of densification was mainly controlled by the current density. A current density of 200 mA mm⁻² was needed to obtain a density in the range of 95%–97%. For comparison, in the case of YSZ, full density is already obtained at a current density of 100 mA mm⁻².⁵⁰ Specimen temperature was measured by optical pyrometer and also estimated by the BBR, showed that 200 mA mm⁻² the specimen reached a temperature of approximately 1400°C. The temperature required to obtain the similar degree of densification of the same powder by conventional free sintering is found to be in a good agreement with the estimated temperature during flash sintering.

In voltage-to-current experiments with DC current, non-uniform grain size distribution along the gauge length of the GDC10 specimens was found. The grain size near the anode is larger by a factor of 10 than the grain size near the cathode. The coarser grain size at the positive side is attributed to the segregation of ions under the DC field, which influence the grain boundary mobility.

The electrical conductivity of the flash sintered and conventional sintered samples were measured using electrochemical impedance spectroscopy (EIS). The total and grain conductivity of both the samples were identical within the margin of error of the analysis, while the grain boundary conductivity of the flash sintered sample was somewhat higher than that of the conventionally sintered sample. Further investigations are necessary to confirm whether the higher grain boundary conductivity is a result of the flash sintering process.

ACKNOWLEDGMENTS

The authors acknowledge funding from the German Science Foundation (DFG), under priority program “Fields Matter” (SPP 1959) under the Grant No. BR 3418/1-1 and BR 3418/1-2.” Furthermore, the authors would like to acknowledge the technical support for the flash sintering experiments and valuable scientific discussions of Dr. Rubens Roberto Ingraci Neto.

ORCID

Tarini Prasad Mishra  <https://orcid.org/0000-0002-3176-5204>
 Christian Lenser  <https://orcid.org/0000-0001-5636-2201>
 Rishi Raj  <https://orcid.org/0000-0001-8556-9797>
 Olivier Guillou  <https://orcid.org/0000-0003-4831-5725>
 Martin Bram  <https://orcid.org/0000-0002-1203-2777>

REFERENCES

- Melchionna M, Fornasiero P. The role of ceria-based nanostructured materials in energy applications. *Mater Today*. 2014;17(7):349–57. <https://doi.org/10.1016/j.mattod.2014.05.005>.
- Möller M, Urban S, Cop P, Weller T, Ellinghaus R, Kleine-Boymann M, et al. Synthesis and physicochemical characterization of Ce_{1-x}Gd_xO_{2-δ}: a case study on the impact of the oxygen storage capacity on the HCl oxidation reaction. *ChemCatChem*. 2015;7(22):3738–47. <https://doi.org/10.1002/cctc.201500712>.
- Trovarelli A. Catalytic properties of ceria and CeO₂-containing materials. *Catalysis Rev.* 1996;38(4):439–520. <https://doi.org/10.1080/01614949608006464>.
- Caravaca A, Picart S, Aouine M, Arab-Chapelet B, Vernoux P, Delahaye T. Development of highly nano-dispersed NiO/GDC catalysts from ion exchange resin templates. *Catalysts*. 2017;7(12):368. <https://doi.org/10.3390/catal7120368>.
- Kašpar J, Fornasiero P, Graziani M. Use of CeO₂-based oxides in the three-way catalysis. *Catal Today*. 1999;50(2):285–98. [https://doi.org/10.1016/S0920-5861\(98\)00510-0](https://doi.org/10.1016/S0920-5861(98)00510-0).
- Eguchi K, Setoguchi T, Inoue T, Arai H. Electrical properties of ceria-based oxides and their application to solid oxide fuel cells. *Solid State Ionics*. 1992;52(1):165–72. [https://doi.org/10.1016/0167-2738\(92\)90102-U](https://doi.org/10.1016/0167-2738(92)90102-U).
- Steele BCH. Appraisal of Ce_{1-y}Gd_yO_{2-y/2} electrolytes for IT-SOFC operation at 500°C. *Solid State Ionics*. 2000;129(1):95–110. [https://doi.org/10.1016/S0167-2738\(99\)00319-7](https://doi.org/10.1016/S0167-2738(99)00319-7).
- Beie H-J, Gnörich A. Oxygen gas sensors based on CeO₂ thick and thin films. *Sensors Actuators B: Chemical*. 1991;4(3):393–9. [https://doi.org/10.1016/0925-4005\(91\)80141-6](https://doi.org/10.1016/0925-4005(91)80141-6).
- Izu N, Shin W, Murayama N, Kanzaki S. Resistive oxygen gas sensors based on CeO₂ fine powder prepared using mist pyrolysis. *Sensors Actuators B: Chemical*. 2002;87(1):95–8. [https://doi.org/10.1016/S0925-4005\(02\)00224-1](https://doi.org/10.1016/S0925-4005(02)00224-1).
- Ramasamy M, Baumann S, Palisaitis J, Schulze-Küppers F, Balaguer M, Kim D, et al. Influence of microstructure and surface activation of dual-phase membrane Ce_{0.8}Gd_{0.2}O_{2-δ}–FeCo₂O₄ on oxygen permeation. *J Am Ceram Soc*. 2016;99(1):349–55. <https://doi.org/10.1111/jace.13938>.
- Chatzichristodoulou C, Søgaard M, Glasscock J, Kaiser A, Foghmoes SPV, Hendriksen PV. Oxygen permeation in thin, dense Ce_{0.9}Gd_{0.1}O_{1.95-δ} membranes II. Experimental determination. *J Electrochem Soc*. 2011;158(5):F73–F83. <https://doi.org/10.1149/1.3559189>.
- Rojek-Wöckner VA, Opitz AK, Brandner M, Mathé J, Bram M. A novel Ni/ceria-based anode for metal-supported solid oxide fuel cells. *J Power Sources*. 2016;328:65–74. <https://doi.org/10.1016/j.jpowsour.2016.07.075>.
- Bischof C, Nenning A, Malleier A, Martetschläger L, Gladbach A, Schafbauer W, et al. Microstructure optimization of nickel/gadolinium-doped ceria anodes as key to significantly increasing power density of metal-supported solid oxide fuel cells. *Int J Hydrogen Energy*. 2019;44(59):31475–87. <https://doi.org/10.1016/j.ijhydene.2019.10.010>.

14. Udomsilp D, Thaler F, Menzler NH, Bischof C, de Haart LGJ, Opitz AK, et al. Dual-phase cathodes for metal-supported solid oxide fuel cells: processing, performance, Durability. *J Electrochem Soc.* 2019;166(8):F506–F510. <https://doi.org/10.1149/2.0561908jes>.
15. Leng YJ, Chan SH, Jiang SP, Khor KA. Low-temperature SOFC with thin film GDC electrolyte prepared in situ by solid-state reaction. *Solid State Ionics.* 2004;170(1):9–15. <https://doi.org/10.1016/j.ssi.2004.02.026>.
16. Jo SH, Muralidharan P, Kim DK. Electrical characterization of dense and porous nanocrystalline Gd-doped ceria electrolytes. *Solid State Ionics.* 2008;178(39):1990–7. <https://doi.org/10.1016/j.ssi.2007.12.076>.
17. Neuhaus K, Dolle R, Wiemhöfer H-D. The effect of transition metal oxide addition on the conductivity of commercially available Gd-doped ceria. *J Electrochem Soc.* 2020;167(4):044507. <https://doi.org/10.1149/1945-7111/ab729b>.
18. Yasuda K, Uemura K, Shiota T. Sintering and mechanical properties of gadolinium-doped ceria ceramics. *J Phys: Conf Ser.* 2012;339:012006. <https://doi.org/10.1088/1742-6596/339/1/012006>.
19. Caisso M, Boulesteix R, Picart S, Maître A, Delahaye T, Ayral A. Investigation of the sintering mechanisms of GDC pellets obtained by the compaction of nanostructured oxide microspheres. *J Am Ceram Soc.* 2017;100(10):4450–60. <https://doi.org/10.1111/jace.14993>.
20. Zhu T, Lin YE, Yang Z, Su D, Ma S, Han M, et al. Evaluation of Li₂O as an efficient sintering aid for gadolinia-doped ceria electrolyte for solid oxide fuel cells. *J Power Sources.* 2014;261:255–63. <https://doi.org/10.1016/j.jpowsour.2014.03.010>.
21. Gil V, Tartaj J, Moure C, Durán P. Sintering, microstructural development, and electrical properties of gadolinia-doped ceria electrolyte with bismuth oxide as a sintering aid. *J Eur Ceram Soc.* 2006;26(15):3161–71. <https://doi.org/10.1016/j.jeurceramsoc.2005.09.068>.
22. He Z, Yuan H, Glasscock JA, Chatzichristodoulou C, Phair JW, Kaiser A, et al. Densification and grain growth during early-stage sintering of Ce_{0.9}Gd_{0.1}O_{1.95–δ} in a reducing atmosphere. *Acta Mater.* 2010;58(11):3860–6. <https://doi.org/10.1016/j.actamat.2010.03.046>.
23. Esposito V, Ni DW, He Z, Zhang W, Prasad AS, Glasscock JA, et al. Enhanced mass diffusion phenomena in highly defective doped ceria. *Acta Mater.* 2013;61(16):6290–300. <https://doi.org/10.1016/j.actamat.2013.07.012>.
24. Ni DW, Glasscock JA, Pons A, Zhang W, Prasad A, Sanna S, et al. Densification of highly defective ceria by high temperature controlled re-oxidation. *J Electrochem Soc.* 2014;161(11):F3072–F3078. <https://doi.org/10.1149/2.0121411jes>.
25. Song J-H, Jung MG, Park HW, Lim H-T. The effect of fabrication conditions for GDC buffer layer on electrochemical performance of solid oxide fuel cells. *Nano-Micro Lett.* 2013;5(3):151–8. <https://doi.org/10.1007/BF03353744>.
26. Mishra TP, Laptev AM, Ziegner M, Sistla SK, Kaletsch A, Broeckmann C, et al. Field-assisted sintering/spark plasma sintering of gadolinium-doped ceria with controlled re-oxidation for crack prevention. *Materials.* 2020;13(14):3184. <https://doi.org/10.3390/ma13143184>.
27. Grasso S, Sakka Y, Maizza G. Electric current activated/assisted sintering (ECAS): a review of patents 1906–2008. *Sci Technol Adv Mater.* 2009;10(5):053001. <https://doi.org/10.1088/1468-6996/10/5/053001>.
28. Olevsky EA, Dudina DV. Flash sintering. Field-assisted sintering: science and applications. Cham, Switzerland: Springer International Publishing; 2018;193–232. <https://doi.org/10.1007/9783-319-76032-2>.
29. Guillou O, Gonzalez-Julian J, Dargatz B, Kessel T, Schierning G, Räthel J, et al. Field-assisted sintering technology/spark plasma sintering: mechanisms, materials, and technology developments: FAST/SPS: mechanisms, materials, and technology developments. *Adv Eng Mater.* 2014;16(7):830–49. <https://doi.org/10.1002/adem.201300409>.
30. Bram M, Laptev AM, Mishra TP, Nur K, Kindermann M, Ihrig M, et al. Application of electric current-assisted sintering techniques for the processing of advanced materials. *Adv Eng Mater.* 2020;22(6):2000051. <https://doi.org/10.1002/adem.202000051>.
31. Cologna M, Rashkova B, Raj R. Flash sintering of nanograin zirconia in <5 s at 850°C. *J Am Ceram Soc.* 2010;93(11):3556–9. <https://doi.org/10.1111/j.1551-2916.2010.04089.x>.
32. Biesuz M, Sglavo VM. Flash sintering of ceramics. *J Eur Ceram Soc.* 2019;39(2):115–43. <https://doi.org/10.1016/j.jeurceramsoc.2018.08.048>.
33. Challenges in Spark Plasma Sintering of Cerium (IV) Oxide - Prasad - 2018 - Ceramic Transactions Series - Wiley Online Library. n.d.
34. Sistla SK, Mishra TP, Deng Y, Kaletsch A, Bram M, Broeckmann C. Polarity-induced grain growth of gadolinium-doped ceria under field-assisted sintering technology/spark plasma sintering (FAST/SPS) conditions. *J Am Ceram Soc.* 2021;104(5):1978–96.
35. Prasad A, Malakkal L, Bichler L, Szpunar J. Challenges in spark plasma sintering of cerium (IV) oxide. Processing, properties, and design of advanced ceramics and composites II. John Wiley & Sons, Ltd. 2018:217–24. <https://doi.org/10.1002/9781119423829.ch19>.
36. Cologna M, Rashkova B, Raj R. Flash sintering of nanograin zirconia in <5 s at 850°C: Rapid Communications of the American Ceramic Society. *J Am Ceram Soc.* 2010;93(11):3556–9. <https://doi.org/10.1111/j.1551-2916.2010.04089.x>.
37. Yu M, Grasso S, McKinnon R, Saunders T, Reece MJ. Review of flash sintering: materials, mechanisms and modelling. *Adv Appl Ceram.* 2017;116(1):24–60. <https://doi.org/10.1080/17436753.2016.1251051>.
38. Dancer CEJ. Flash sintering of ceramic materials. *Mater Res Express.* 2016;3(10):102001. <https://doi.org/10.1088/2053-1591/3/10/102001>.
39. Raj R. Analysis of the power density at the onset of flash sintering. *J Am Ceram Soc.* 2016;99(10):3226–32. <https://doi.org/10.1111/jace.14178>.
40. Becker MZ, Shomrat N, Tsur Y. Recent advances in mechanism research and methods for electric-field-assisted sintering of ceramics. *Adv Mater.* 2018;30(41):1706369. <https://doi.org/10.1002/adma.201706369>.
41. Chaim R, Chevallier G, Weibel A, Estournès C. Flash sintering of dielectric nanoparticles as a percolation phenomenon through a softened film. *J Appl Phys.* 2017;121(14):145103. <https://doi.org/10.1063/1.4980853>.
42. da Silva JGP, Al-Qureshi HA, Keil F, Janssen R. A dynamic bifurcation criterion for thermal runaway during the flash sintering of ceramics. *J Eur Ceram Soc.* 2016;36(5):1261–7. <https://doi.org/10.1016/j.jeurceramsoc.2015.11.048>.
43. Muccillo R, Muccillo ENS. Electric field-assisted flash sintering of tin dioxide. *J Eur Ceram Soc.* 2014;34(4):915–23. <https://doi.org/10.1016/j.jeurceramsoc.2013.09.017>.

44. Grimley CA, Prette ALG, Dickey EC. Effect of boundary conditions on reduction during early stage flash sintering of YSZ. *Acta Mater.* 2019;174:271–8. <https://doi.org/10.1016/j.actamat.2019.05.001>.
45. Pkm K, Yadav D, Lebrun J-M, Raj R. Flash sintering with current rate: a different approach. *J Am Ceram Soc.* 2019;102(2):823–35. <https://doi.org/10.1111/jace.16037>.
46. Charalambous H, Jha SK, Christian KH, Lay RT, Tsakalakos T. Flash sintering using controlled current ramp. *J Eur Ceram Soc.* 2018;38(10):3689–93. <https://doi.org/10.1016/j.jeurceramsoc.2018.04.003>.
47. Phuah XL, Wang H, Charalambous H, Jha SK, Tsakalakos T, Zhang X, et al. Comparison of the grain growth behavior and defect structures of flash sintered ZnO with and without controlled current ramp. *Scripta Mater.* 2019;162:251–5. <https://doi.org/10.1016/j.scriptamat.2018.11.009>.
48. Mishra TP, Neto RRI, Raj R, Guillon O, Bram M. Current-rate flash sintering of gadolinium doped ceria: microstructure and defect generation. *Acta Mater.* 2020;189:145–53. <https://doi.org/10.1016/j.actamat.2020.02.036>.
49. Mishra TP, Avila V, Neto RRI, Bram M, Guillon O, Raj R. On the role of Debye temperature in the onset of flash in three oxides. *Scripta Mater.* 2019;170:81–4. <https://doi.org/10.1016/j.scriptamat.2019.05.030>.
50. Francis JSC, Raj R. Influence of the field and the current limit on flash sintering at isothermal furnace temperatures. *J Am Ceram Soc.* 2013;96(9):2754–8. <https://doi.org/10.1111/jace.12472>.
51. Lebrun J-M, Raj R. A first report of photoemission in experiments related to flash sintering. *J Am Ceram Soc.* 2014;97(8):2427–30. <https://doi.org/10.1111/jace.13130>.
52. Biesuz M, Luchi P, Quaranta A, Martucci A, Sglavo VM. Photoemission during flash sintering: an interpretation based on thermal radiation. *J Eur Ceram Soc.* 2017;37(9):3125–30. <https://doi.org/10.1016/j.jeurceramsoc.2017.03.050>.
53. Yadav D, Raj R. Two unique measurements related to flash experiments with yttria-stabilized zirconia. *J Am Ceram Soc.* 2017;100(12):5374–8. <https://doi.org/10.1111/jace.15114>.
54. Schmerbauch C, Gonzalez-Julian J, Röder R, Ronning C, Guillon O. Flash sintering of nanocrystalline zinc oxide and its influence on microstructure and defect formation. *J Am Ceram Soc.* 2014;97(6):1728–35. <https://doi.org/10.1111/jace.12972>.
55. Biesuz M, Sglavo VM. Flash sintering of alumina: effect of different operating conditions on densification. *J Eur Ceram Soc.* 2016;36(10):2535–42. <https://doi.org/10.1016/j.jeurceramsoc.2016.03.021>.
56. Jongmanns M, Raj R, Wolf DE. Generation of Frenkel defects above the Debye temperature by proliferation of phonons near the Brillouin zone edge. *New J Phys.* 2018;20(9):093013. <https://doi.org/10.1088/1367-2630/aadd5a>.
57. Todd RI, Zapata-Solvas E, Bonilla RS, Sneddon T, Wilshaw PR. Electrical characteristics of flash sintering: thermal runaway of Joule heating. *J Eur Ceram Soc.* 2015;35(6):1865–77. <https://doi.org/10.1016/j.jeurceramsoc.2014.12.022>.
58. Zhang Y, Jung J-I, Luo J. Thermal runaway, flash sintering and asymmetrical microstructural development of ZnO and ZnO–Bi₂O₃ under direct currents. *Acta Mater.* 2015;94:87–100. <https://doi.org/10.1016/j.actamat.2015.04.018>.
59. Chaim R. Liquid film capillary mechanism for densification of ceramic powders during flash sintering. *Materials.* 2016;9(4):280. <https://doi.org/10.3390/ma9040280>.
60. Lebrun J-M, Hellberg CS, Jha SK, Kriven WM, Steveson A, Seymour KC, et al. In-situ measurements of lattice expansion related to defect generation during flash sintering. *J Am Ceram Soc.* 2017;100(11):4965–70. <https://doi.org/10.1111/jace.15071>.
61. Narayan J. A new mechanism for field-assisted processing and flash sintering of materials. *Scripta Mater.* 2013;69(2):107–11. <https://doi.org/10.1016/j.scriptamat.2013.02.020>.
62. Naik KS, Sglavo VM, Raj R. Flash sintering as a nucleation phenomenon and a model thereof. *J Eur Ceram Soc.* 2014;34(15):4063–7. <https://doi.org/10.1016/j.jeurceramsoc.2014.04.043>.
63. Ren K, Liu J, Wang Y. Flash sintering of yttria-stabilized zirconia: fundamental understanding and applications. *Scripta Mater.* 2020;187:371–8. <https://doi.org/10.1016/j.scriptamat.2020.06.040>.
64. Biesuz M, Sglavo VM. Electric forces effect on field-assisted sintering. *J Eur Ceram Soc.* 2020;40(15):6259–65. <https://doi.org/10.1016/j.jeurceramsoc.2020.06.069>.
65. Spiridigliozi L, Pinter L, Biesuz M, Dell'Agli G, Accardo G, Sglavo VM. Gd/Sm-Pr co-doped ceria: a first report of the precipitation method effect on flash sintering. *Materials.* 2019;12(8):1218. <https://doi.org/10.3390/ma12081218>.
66. Spiridigliozi L, Biesuz M, Dell'Agli G, Di Bartolomeo E, Zurlo F, Sglavo VM. Microstructural and electrical investigation of flash-sintered Gd/Sm-doped ceria. *J Mater Sci.* 2017;52(12):7479–88. <https://doi.org/10.1007/s10853-017-0980-2>.
67. Jiang T, Wang Z, Zhang J, Hao X, Rooney D, Liu Y, et al. Understanding the flash sintering of rare-earth-doped ceria for solid oxide fuel cell. *J Am Ceram Soc.* 2015;98(6):1717–23. <https://doi.org/10.1111/jace.13526>.
68. Hao X, Liu Y, Wang Z, Qiao J, Sun K. A novel sintering method to obtain fully dense gadolinia doped ceria by applying a direct current. *J Power Sources.* 2012;210:86–91. <https://doi.org/10.1016/j.jpowsour.2012.03.006>.
69. Cologna M, Francis JSC, Raj R. Field assisted and flash sintering of alumina and its relationship to conductivity and MgO-doping. *J Eur Ceram Soc.* 2011;31(15):2827–37. <https://doi.org/10.1016/j.jeurceramsoc.2011.07.004>.
70. Schönleber M, Klotz D, Ivers-Tiffée E. A method for improving the robustness of linear Kramers-Kronig validity tests. *Electrochim Acta.* 2014;131:20–7. <https://doi.org/10.1016/j.electacta.2014.01.034>.
71. Hong SJ, Virkar AV. Lattice parameters and densities of rare-earth oxide doped ceria electrolytes. *J Am Ceram Soc.* 1995;78(2):433–9. <https://doi.org/10.1111/j.1151-2916.1995.tb08820.x>.
72. Mishra TP, Neto RRI, Speranza G, Quaranta A, Sglavo VM, Raj R, et al. Electronic conductivity in gadolinium doped ceria under direct current as a trigger for flash sintering. *Scripta Mater.* 2020;179:55–60. <https://doi.org/10.1016/j.scriptamat.2020.01.007>.
73. Baraki R, Schwarz S, Guillon O. Effect of electrical field/current on sintering of fully stabilized zirconia. *J Am Ceram Soc.* 2012;95(1):75–8. <https://doi.org/10.1111/j.1551-2916.2011.04980.x>.
74. Kirchheim R. Incubation time for flash sintering as caused by internal reactions, exemplified for yttria stabilized zirconia. *Acta Mater.* 2019;175:361–75. <https://doi.org/10.1016/j.actamat.2019.06.030>.
75. Dirkmann S, Kaiser J, Wenger C, Mussenbrock T. Filament growth and resistive switching in hafnium oxide memristive devices. *ACS Appl Mater Interfaces.* 2018;10(17):14857–68. <https://doi.org/10.1021/acsami.7b19836>.
76. Sun W, Gao B, Chi M, Xia Q, Yang JJ, Qian HE, et al. Understanding memristive switching via in situ characterization

- and device modeling. *Nat Commun.* 2019;10(1):3453. <https://doi.org/10.1038/s41467-019-11411-6>.
77. Ganduglia-Pirovano MV, Da Silva JLF, Sauer J. Density-functional calculations of the structure of near-surface oxygen vacancies and electron localization on CeO₂(111). *Phys Rev Lett.* 2009;102(2):026101. <https://doi.org/10.1103/PhysRevLett.102.026101>.
78. Wang S, Kobayashi T, Dokiya M, Hashimoto T. Electrical and ionic conductivity of Gd-doped ceria. *J Electrochem Soc.* 2000;147(10):3606. <https://doi.org/10.1149/1.1393946>.
79. Terauds K, Lebrun J-M, Lee H-H, Jeon T-Y, Lee S-H, Je JH, et al. Electroluminescence and the measurement of temperature during Stage III of flash sintering experiments. *J Eur Ceram Soc.* 2015;35(11):3195–9. <https://doi.org/10.1016/j.jeurceramsoc.2015.03.040>.
80. Raj R. Joule heating during flash-sintering. *J Eur Ceram Soc.* 2012;32(10):2293–301. <https://doi.org/10.1016/j.jeurceramsoc.2012.02.030>.
81. Grasso S, Sakka Y, Rendtorff N, Hu C, Maizza G, Borodianska H, et al. Modeling of the temperature distribution of flash sintered zirconia. *J Ceram Soc Jpn.* 2011;119(1386):144–6. <https://doi.org/10.2109/jcersj2.119.144>.
82. Liu G, Liu D, Liu J, Gao Y, Wang Y. Asymmetric temperature distribution during steady stage of flash sintering dense zirconia. *J Eur Ceram Soc.* 2018;38(7):2893–6. <https://doi.org/10.1016/j.jeurceramsoc.2018.02.012>.
83. Qin W, Majidi H, Yun J, van Benthem K. Electrode effects on microstructure formation during FLASH sintering of yttrium-stabilized zirconia. *J Am Ceram Soc.* 2016;99(7):2253–9. <https://doi.org/10.1111/jace.14234>.
84. Charalambous H, Jha SK, Wang H, Phuah XL, Wang H, Tsakalakos T. Inhomogeneous reduction and its relation to grain growth of titania during flash sintering. *Scripta Mater.* 2018;155:37–40. <https://doi.org/10.1016/j.scriptamat.2018.06.017>.
85. Demirskyi D, Vasylkiv O. Hot-spots generation, exaggerated grain growth and mechanical performance of silicon carbide bulks consolidated by flash spark plasma sintering. *J Alloy Compd.* 2017;691:466–73. <https://doi.org/10.1016/j.jallcom.2016.08.234>.
86. Biesuz M, Pinter L, Saunders T, Reece M, Binner J, Sglavo V, et al. Investigation of electrochemical, optical and thermal effects during flash sintering of 8YSZ. *Materials.* 2018;11(7):1214. <https://doi.org/10.3390/ma11071214>.
87. Chun J, Martin M, Yoo H-I. Electrotransport-induced unmixing and decomposition of ternary oxides. *J Appl Phys.* 2015;117(12):124504. <https://doi.org/10.1063/1.4915626>.
88. Sternlicht H, Rheinheimer W, Mehlmann A, Rothschild A, Hoffmann MJ, Kaplan WD. The mechanism of grain growth at general grain boundaries in SrTiO₃. *Scripta Mater.* 2020;188:206–11. <https://doi.org/10.1016/j.scriptamat.2020.07.015>.
89. Sternlicht H, Rheinheimer W, Hoffmann MJ, Kaplan WD. The mechanism of grain boundary motion in SrTiO₃. *J Mater Sci.* 2016;51(1):467–75. <https://doi.org/10.1007/s10853-015-9058-1>.
90. Rheinheimer W, Parras JP, Preusker J-H, Souza RAD, Hoffmann MJ. Grain growth in strontium titanate in electric fields: The impact of space-charge on the grain-boundary mobility. *J Am Ceram Soc.* 2019;102(6):3779–90. <https://doi.org/10.1111/jace.16217>.
91. Zhang J, Lenser C, Menzler NH, Guillon O. Comparison of solid oxide fuel cell (SOFC) electrolyte materials for operation at 500°C. *Solid State Ionics.* 2020;344:115138. <https://doi.org/10.1016/j.ssi.2019.115138>.

SUPPORTING INFORMATION

Additional supporting information may be found online in the Supporting Information section.

How to cite this article: Mishra TP, Lenser C, Raj R, Guillon O, Bram M. Development of a processing map for safe flash sintering of gadolinium-doped ceria. *J Am Ceram Soc.* 2021;104:4316–4328. <https://doi.org/10.1111/jace.17847>